Progress In Electromagnetics Research, Vol. 177, 85–94, 2023

Terahertz Plasmonic Metagrating Design Simultaneously Enabling Broadband Extraordinary Transmission and Field Enhancement

Chi Wang[1, 3], Shurun Tan[2, 4], Xiao Lin[1, 3], Hongsheng Chen[1, 3, *], and Fei Gao[1, 3, *]

Abstract—Metagratings, consisting of subwavelength-aperture arrays (SAAs), provide a powerful platform to manipulate electromagnetic waves. Typical examples include extraordinary optic transmission (EOT) in the far field and field enhancements (FEs) in the near field. These capabilities promise applications in beam steering and wave-matter interactions, but are not extended to broad bandwidth simultaneously. Here, we transplant the concept of broadband light harvesting devices from optic to terahertz frequency and by exploring one-dimensional arrays of spirally textured metallic cylinders supporting multiple designer localized surface plasmon resonances. Theoretical analysis reveals that the interaction between localized plasmons leads to the broadband THz EOTs in the far field as well as large field enhancements in the near field. The bandwidth of the EOT and the magnitude of field enhancements can be flexibly designed by changing the geometry of the plasmonic-like resonators. This design promises applications in THz broadband beam-steering, absorbers, and sensing, topological devices.

1. INTRODUCTION

Metagratings, consisting of subwavelength-aperture arrays (SAAs), are fertile grounds in investigating exotic wave phenomena, ranging from optics [1–5] to acoustics [6–9]. In 1998, Ebbesen *et al.* [10] shone light on metallic SAAs and observed a higher transmission than the prediction of the standard aperture theory, thus naming the phenomenon as extraordinary optical transmission (EOT). Such exotic phenomena are promising in far-field optic applications, such as beam collimations [2]. Due to the universality of wave physics, the exotic phenomena have also been transferred into lower frequency ranges, e.g., terahertz frequencies [11–25]. Usually, such EOTs are narrowband under normal incidences [12–22], due to the collective resonances in subwavelength apertures. The resonances in subwavelength aperture gives rise to large field enhancements (FEs) (shown as the second quadrant in Fig. 1) and promises applications in wave-matter interactions, e.g., absorbers, and nonlinear phenomena. Therefore, the metagratings show promising applications in both far field and near field.

Many efforts have been devoted to increase the operational bandwidths of metagratings. One approach explores the grazing incidences [26–29]. The broadband EOTs have been observed, which are attributed to the impedance matching between SAAs with environments without arousing any resonances, thus without near-field FEs (shown as the fourth quadrant in Fig. 1). This approach has been experimentally demonstrated in THz frequencies [23–25]. So far, the broad operational bandwidth has not been endowed to far-field EOT and near-field FEs, simultaneously on a single metagrating.

Received 10 March 2023, Accepted 10 June 2023, Scheduled 19 June 2023

* Corresponding author: Hongsheng Chen (hansomchen@zju.edu.cn), Fei Gao (gaofeizju@zju.edu.cn).

[1] Interdisciplinary Center for Quantum Information, State Key Laboratory of Modern Optical Instrumentation, College of Information Science and Electronic Engineering, Zhejiang University, Hangzhou 310027, China. [2] Zhejiang University-University of Illinois at Urbana-Champaign Institute, Zhejiang University, Haining, Zhejiang 314400, China. [3] International Joint Innovation Center, Zhejiang University, Haining 314400, China. [4] Department of Electrical and Computer Engineering, University of Illinois at Urbana-Champaign, Urbana, IL 61801, USA.

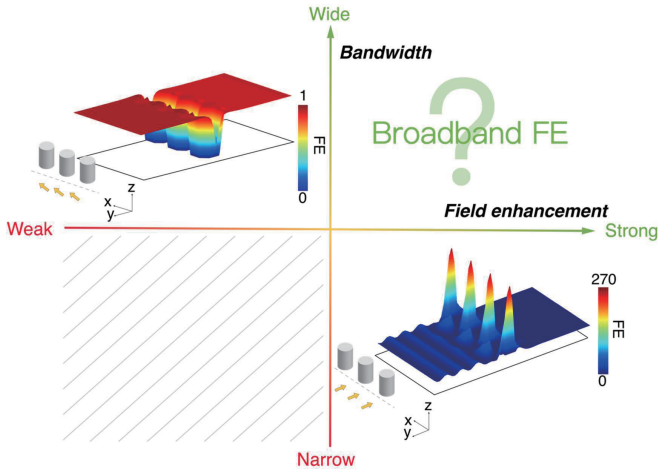

Figure 1. Terahertz broadband EOT with FE simultaneously. The trade-off between bandwidth-FE in conventional metagrating consisting of perfect electric conductor (PEC) cylinders. The second quadrant shows broadband EOT without FE, under grazing incidence. The fourth quadrant shows narrow band EOT with FE, under normal incidence.

Here, we propose a type of metagratings, being a one-dimensional array of spirally textured cylinders. Each cylinder hosts multiple designer localized surface plasmonic (DLSP) resonances, rather than being non-resonant scatterers as in conventional metagratings. Multiple scatterings hybridizing these DLSPs lead to the broadband EOTs in the far field, as well as FEs in the near field. Such metagratings provide a platform to transplant the concept of broadband light harvesting devices from optic [3, 4] to terahertz frequency. The bandwidth and magnitude of FEs are also designed by changing the spiral angles of the DLSP resonators.

2. THEORETICAL MODEL

The one-dimensional metagrating is an array of cylindrical DLSP resonators situated in air. Fig. 2(a) exhibits the geometry of an individual DLSP resonator, which is a metallic cylinder textured with logarithmic spirals [30]. The inner, outer radii, and spiral angle of the resonator are denoted with r, R, and θ, respectively. The outer arc and period of the groove are a and d, respectively. The number of grooves is large (such as 36 in Fig. 2(a)), which ensures that the size of each groove is in deep subwavelength. Therefore, electromagnetic properties of an individual DLSP resonator can be understood with the effective core-shell model of continuous media proposed by Liao *et al.* [30]. In the THz region, the metal core is approximated as a perfect electric conductor (PEC). Under transverse magnetic (TM) waves, the effective permittivity and permeability [30] of the shell are expressed as $\varepsilon^{-1} = \frac{a}{2d}\begin{bmatrix} 1-\cos 2\theta & -\sin 2\theta \\ -\sin 2\theta & 1+\cos 2\theta \end{bmatrix}\varepsilon_0$ and $\mu_z^{-1} = \frac{d}{a}\mu_0$, respectively, where ε_0 and μ_0 are permittivity and permeability of air. With such a continuous model, cylindrical scattering theory [31] is applicable, although the effective permittivity is anisotropic.

As shown in the inset of Fig. 1, the array is periodic in the x-direction with period h and is uniform in the z-direction. The centre of the l-th cylinder is at $x = lh$ and $y = 0$. The corresponding local cylindrical coordinates are denoted by $\rho_l = \sqrt{(x-lh)^2 + y^2}$ and $\cos\phi_l = (x-lh)/\rho_l$. We investigate a two-dimensional transmission problem with the multiple scattering theory (MST) [32], by impinging a TM plane wave at incidence angle β. Let the magnetic field $\mathbf{H}^{in}(x, y)$ of the incident wave with unit amplitude. Then, in the 0-th cylindrical coordinate system, $\mathbf{H}^{in}(x, y)$ is expressed as follows.

$$\mathbf{H}^{in}(xy) = \sum_m a_m^{in} J_m\left(k_0\rho_0\right) e^{im\varphi_0} \tag{1}$$

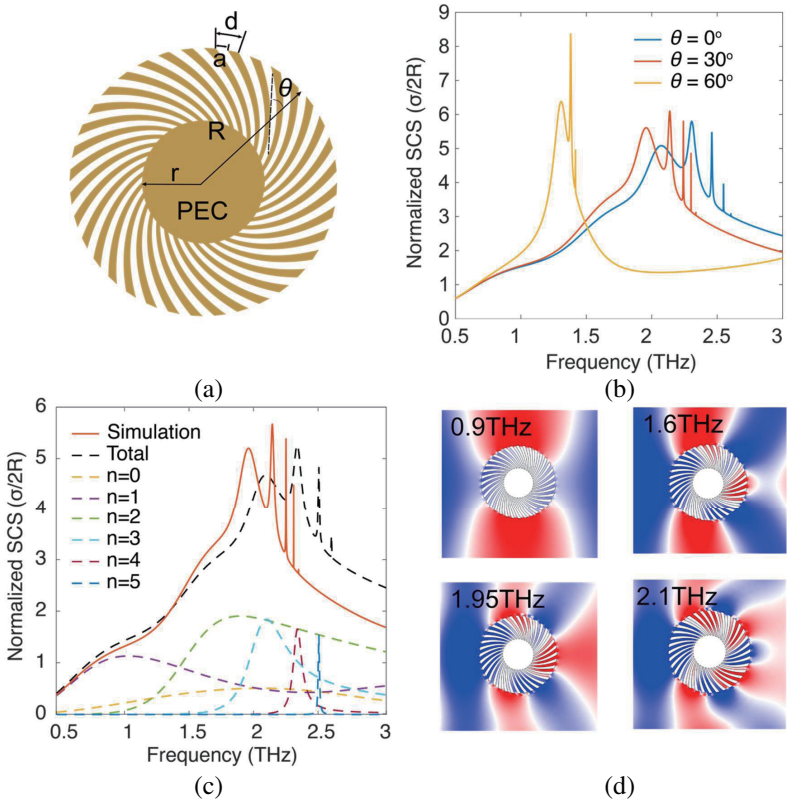

Figure 2. THz designer localized surface plasmonic (DLSP) resonator. (a) The schematic of a DLSP resonator. R and r denote the inner radius and outer radius respectively. θ represents the angle of logarithmic spiral. (b) The simulated normalized SCS spectra of three resonators with different spiral angle $\theta = 0°$, $30°$, and $60°$. We take $r = 20\,\mu\text{m}$, $R = 50\,\mu\text{m}$, respectively. (c) Normalized SCS of the DLSP with $\theta = 30°$. Red solid line denotes the result by full wave simulation, and black dashed line for effective media theory. The other lines represent the SCS contribution of different resonances ($n = 0$, 1, 2, 3, 4, 5), respectively. (d) The corresponding field distributions of E_y at frequencies of the resonance peaks in (c).

where $a_m^{in} = (-i)^m e^{-im(\pi/2-\beta)}$, $J_m(\cdot)$ represents the m-th order Bessel function, and k_0 is the wavenumber in air. Then the scattered field $\mathbf{H}^{SC}(x, y)$ outside the DLSP array is expressed with an infinite sum of cylindrical waves outgoing from the center in each unit. Applying Floquet theorem [33], $\mathbf{H}^{SC}(x, y)$ is expressed as follows:

$$\mathbf{H}^{SC}(xy) = \sum_{l=-\infty}^{\infty} \sum_{m=-\infty}^{\infty} \mathbf{H}_{l,m}^{SC} b_m^0 e^{-ilk_0 h \cdot \sin\beta} \tag{2}$$

$$\mathbf{H}_{l,m}^{SC}(xy) = H_m^{(1)}(k_0\rho_l)\, e^{im\varphi_l} \tag{3}$$

where $H_m^{(1)}$ is the m-th order Hankel function of the first kind, and b_m^0 represents the amplitude of the m-th order cylindrical wave scattered from the 0-th unit. We unify the local cylindrical coordinates with that of 0-th unit cell, by using the addition theorem [33] of Hankel functions,

$$H_m^{(1)}(k_0\rho_l)\, e^{im\varphi_l} = \sum_{n=-\infty}^{\infty} H_{n-m}^{(1)}(k_0 lh)\, e^{-i(n-m)\varphi'} J_n(k_0\rho_0)\, e^{in\varphi_0} \tag{4}$$

where φ' is the polar angle of the l-th cylinder relative to the zeroth one, i.e., $\varphi' = 0$ ($l > 0$) and $\varphi' = \pi$

($l < 0$). The total field in the air is

$$\mathbf{H}(x,y) = \sum_m a_m^{in} J_m(k_0\rho_0)\, e^{im\varphi_0} + \sum_m \sum_n S_{m-n} b_m^0 J_m(k_0\rho_0)\, e^{im\varphi_0} \tag{5}$$

where $S_{m-n} = [1+(-1)^{m-n}] \cdot \sum_{l=1}^{\infty} H_{m-n}^{(1)}(k_0 lh) e^{-ilk_0 h\cdot\sin\beta}$. Since the sum of this expression converges very slowly, it is usually converted to an integral form of the lattice sum [33]. Eq. (5) can be treated as incident waves impinged on the 0-th unit cell, where the amplitude of the total incident waves is

$$a_m^0 = a_m^{in} + \sum_n S_{m-n} b_m^0 \tag{6}$$

For an individual cylinder, we have $b_m = D_m a_m$, where D_m depending on the constitutive parameters of the cylinder is determined by boundary conditions. Therefore, Eq. (6) is converted into

$$b_m^{(0)} = D_m \cdot \sum\nolimits_n S_{m-n} b_n^{(0)} + D_m \cdot a_m^{in} \tag{7}$$

We transform the Bessel functions into plane waves and express the field in the transmitted region as [34]

$$\mathbf{H}_t(x,y) = \sum_{\nu=-\infty}^{\infty} \left(\delta_{\nu 0} + \sum_m q_{v,m} b_m \right) \cdot e^{i(k_{xv}x - k_{yv}y)} \tag{8}$$

where δ_{v0} is the Kronecker symbol, and $\nu \in Z$ represents different diffraction orders. The wavevector of the νth-order diffracted wave is $k_\nu = (k_{xv},\ k_{yv})$, $k_{xv} = -k\sin\beta + 2\nu\pi/(lh)$. $q_{v,m} = \begin{cases} \frac{2(-i)^m (k_{xv} - ik_{yv})^m}{R_l k_y k_0^n}, m \geq 0 \\ \frac{2(i)^{-m}(k_{xv}+ik_{yv})^{-m}}{R_l k_{yv} k_0^{-m}}, m < 0 \end{cases}$ describes the transformation from the mth-order cylindrical harmonics to the plane waves. Only waves with real $k_{yv} = \sqrt{k_0^2 - k_{xv}^2}$ can propagate to far field and contribute to transmission. The v-order transmission t_ν is given as:

$$t_\nu = \left(\frac{k_{yv}}{k_0 \cos\beta} \right)^{\frac{1}{2}} \left(\delta_{\nu 0} + \sum_m q_{v,m} b_m \right) \tag{9}$$

3. RESULTS AND DISCUSSION

We firstly show the numerical scattering cross section (SCS) of individual DLSP resonator with different spiral angles θ, by using finite element solver COMSOL Multiphysics. As shown in Fig. 2(b), each resonator shows multiple resonance peaks in their corresponding SCS spectra. Increasing the spiral angle θ, resonance peaks are closer in spectra. We then explain the numerical SCS spectra by comparing them with the analytical SCS obtained with above core-shell model of effective constitutive parameters. According to the cylindrical scattering theory [31], the analytical SCS σ is expressed with $\sigma = \frac{4}{k_0} \sum_{m=-\infty}^{\infty} |D_m a_m|^2$, where $a_m = (-i)^n$, and $D_m = (-1)^m \frac{\frac{a}{d} J_m(k_0 R) p - \frac{q}{\cos\theta} J_m'(k_0 R)}{\frac{a}{d} H_m^{(1)}(k_0 R) p - \frac{q}{\cos\theta} H_m^{(1)'}(k_0 R)}$. p and q are expressed as

$$\begin{cases} p = J_1\left(\frac{k_0 R}{\cos\theta}\right) Y_1\left(\frac{k_0 R}{\cos\theta}\right) - J_1\left(\frac{k_0 R}{\cos\theta}\right) Y_1\left(\frac{k_0 r}{\cos\theta}\right) \\ q = J_0\left(\frac{k_0 R}{\cos\theta}\right) Y_1\left(\frac{k_0 r}{\cos\theta}\right) - J_1\left(\frac{k_0 r}{\cos\theta}\right) Y_0\left(\frac{k_0 R}{\cos\theta}\right) \end{cases} \tag{10}$$

where $Y_m(\cdot)$ represents the m-th order Neumann function. The detailed derivations can also be found in [30]. Taking the typical cylinder (the inner radius $r = 20\,\mu\text{m}$, outer radius $R = 50\,\mu\text{m}$, spiral angle $\theta = 30°$) as an example, its analytical SCS is shown in Fig. 2(c). The theoretical SCS is well consistent with the numerical one, although the theoretical one shows a frequency shift with respect to the numerical one, since the effective media model does not include the nonlocal effect [30] in the

practical structure. Decomposing the total SCS into contributions of different-order cylindrical waves, higher-frequency resonance peaks are dominated by higher-order cylindrical waves. This phenomenon is further validated with mode patterns from simulations shown in Fig. 2(d). The effective permittivity of the shell does not explicitly show in Eq. (10) but manifests itself as the related spiral angle θ, in the arguments in both Bessel and Neumann functions. In the effective shell, the wavenumber $k_s = k_0/\cos\theta$ increases during increasing θ; therefore, the shell behaves as a high-index material. This analysis further confirms the phenomenon in Fig. 2(b), where resonance peaks redshift during increasing θ.

We further reveal the transmission of a one-dimensional array of DLSP resonators (as shown in Fig. 3(a)), under normal incidence ($\beta = \pi/2$). Neighboring resonators are separated by air gaps of size $g = 1\,\mu\text{m}$, which makes sure that the grating period $h = 2R + g$ is in subwavelength. The transmission is dominated by the 0th order ($\nu = 0$) and expressed as

$$t = 1 + \sum_{m=-N_{CO}}^{N_{CO}} q_{0,m} \cdot b_m \tag{11}$$

where N_{co} represents the cutoff orders. The theoretical spectrum exhibits a broad band with extraordinary high transmission, which is consistent with the numerical one in Fig. 3(b). Both them show several perfect transmission peaks. To reveal the underlying mechanism of the broadband EOT, we turn to Eq. (7), which describes the coupling between cylindrical modes. We rewrite the equation

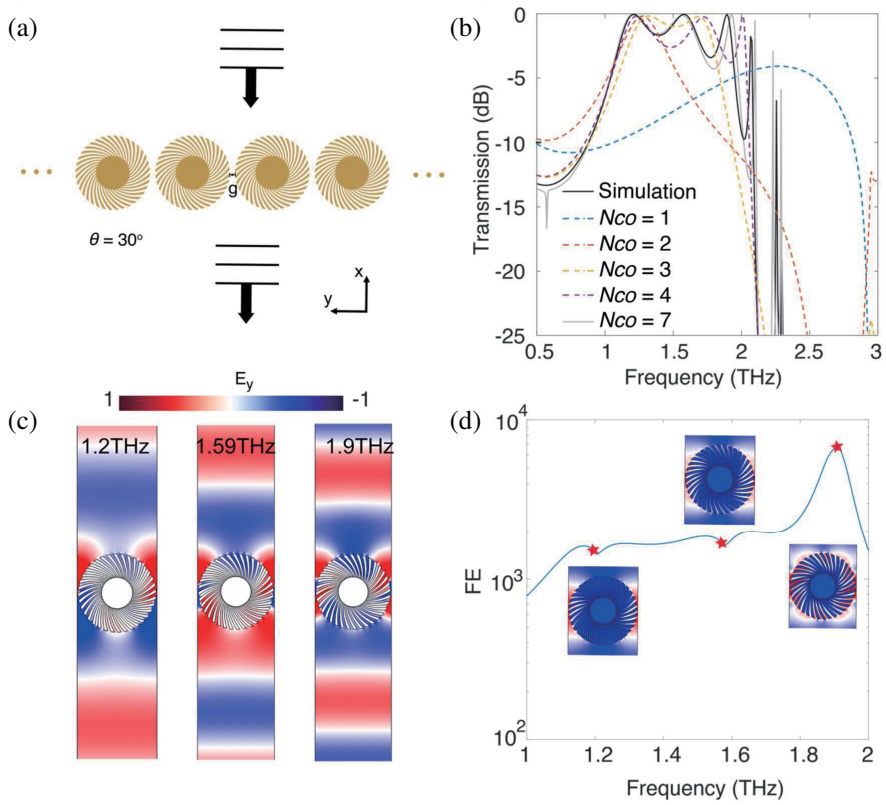

Figure 3. Simultaneous EOT and FE on the THz design-plasmonic metagrating. (a) The metagrating with gap $g = 1\,\mu\text{m}$ and the spiral angle $\theta = 30°$. (b) The transmission through the DLSP metagrating, where the black solid curve denotes the simulated transmission, the dashed lines of different colors represent the transmission calculated with different cutoff mode orders $N_{co} = 1$, 2, 3, 4, 7, respectively. (c) Simulated electric field patterns corresponding to the three prefect transmissions at 1.2 THz, 1.59 THz and 1.9 THz, in Fig. 2(b) respectively. (d) The field enhancement at the middle of the gap. The three red stars denotes the frequencies of perfect transmissions.

as matrix form below and further find the scattering coefficients b_m of each order.

$$\begin{bmatrix} b^{(0)}_{-N_{CO}} \\ \vdots \\ b^{(0)}_{N_{CO}} \end{bmatrix} = \overline{\overline{D}} \cdot \overline{\overline{S}} \cdot \begin{bmatrix} b^{(0)}_{-N_{CO}} \\ \vdots \\ b^{(0)}_{N_{CO}} \end{bmatrix} + \overline{\overline{D}} \cdot \begin{bmatrix} a^{(0)}_{-N_{CO}} \\ \vdots \\ a^{(0)}_{N_{CO}} \end{bmatrix} \tag{12}$$

Theoretical spectra are obtained with Eq. (11) by taking cutoff orders N_{co}. Compared with $N_{co} = 1$, the spectrum of $N_{co} = 2$ in Fig. 3(b) starts to show perfect transmission at $f_1 = 1.2$ THz. It means that the five lowest-order modes couple with each other and further interfere constructively to form the first perfect transmission. Similarly, spectra result with $N_{co} = 3$ and $N_{co} = 4$ explains the origins of perfect transmissions at higher frequencies. Such mode couplings also make the frequency regions between perfect transmission peaks show high transmission, thus rendering the broadband EOT. When $N_{co} = 7$, the theoretical curve converges to the numerical one in Fig. 3(b), since an accurate description requires more orders of modes to be summed. Taking the frequencies at perfect transmissions, we show the numerical field patterns (in Fig. 3(c)) of one unit cell with periodic boundary along the y-direction. The fields in both the incident and transmitted regions in Fig. 3(c) show near-plane wave fronts with equal amplitude. They further confirm the above analysis.

In the EOT band, we further look into the near fields around the gaps. Over the whole EOT band, the field enhancements (FEs) in the gap are around 1700 folds (as shown in Fig. 3(d)), with respect to the amplitude of the incident wave. At 1.9 THz, the maximum FE is around 7000 times. The incident waves are mostly/totally squeezed into the narrow air gaps, thus inducing such large FEs in the near field. These near-field FEs do not occur along with the broadband EOTs based on impedance matching [8, 14–17, 21].

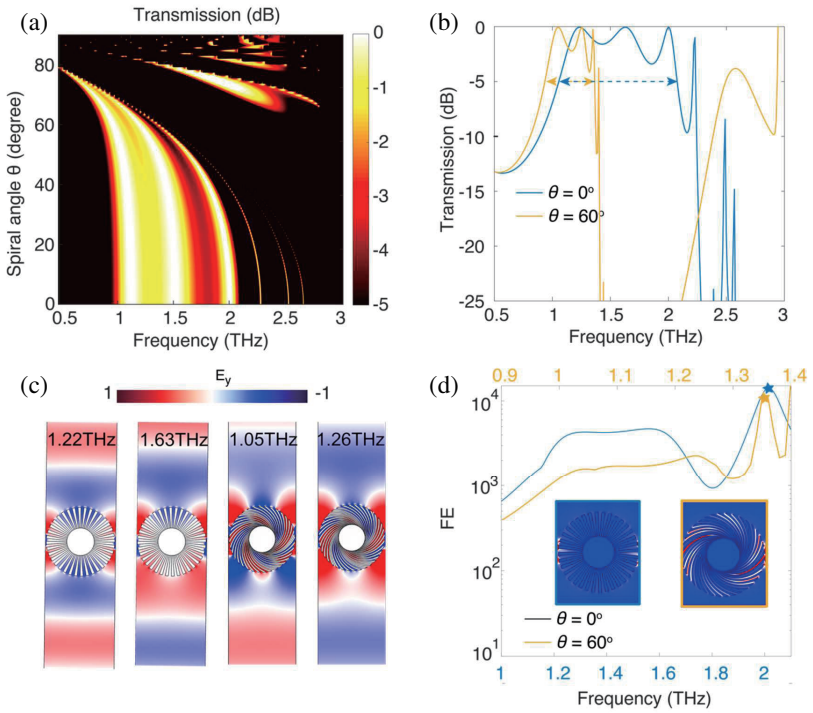

Figure 4. Designing broadband EOT and FE with spiral angles. (a) The calculated phase diagram T (θ, f). (b) The transmission spectra of two different metagratings with $\theta = 0°$ and 60°, respectively. The −5-dB bandwidth is marked as dashed lines. (c) Simulated field patterns of the metagratings with $\theta = 0°$ @ 1.22 THz, and 1.63 THz, and $\theta = 60°$ @ 1.05 THz, and 1.26 THz. (d) The field enhancement at the middle of the gap. The lower and upper horizontal axis are for the $\theta = 0°$, and $\theta = 60°$ metagratings, respectively.

Interestingly, the spiral angle of groove arms behaves as a degree of freedom for designing the broadband FEs. According to Eq. (11), the phase diagram of transmission is shown in Fig. 4(a), by sweeping spiral angle θ and frequency f. The perfect transmissions redshift, and the EOT bandwidth decreases as θ increases. Intuitively, the larger θ, corresponding to larger groove depths, are equivalent to the fillings of high-index materials [35–37]. DLSP with larger θ can redshift resonance frequencies and confine fields more tightly, as filling with higher-index materials. Quantitatively as shown in Fig. 4(b), when the spiral angle θ increases from 0° to 60°, the center frequency of EOT redshifts from 1.63 THz to 1.16 THz, and the −5 dB bandwidth drops from 1.84 kHz to 0.72k Hz. The simulated field patterns in Fig. 4(c) further verify the broadband EOTs. The bandwidth of FEs also decreases when the spiral angle θ increases from 0° to 60°, while the FEs of both metagratings are higher than 1000 times as shown in Fig. 4(d).

Last but not least, we investigate the incidence-angle dependence of the broadband EOT and FE. According to Eq. (9), we obtain the phase diagram of the transmission by sweeping incident angle β and frequency f. Fig. 5(a) shows three angular bands of perfect transmission, between which transmission is higher than −5 dB. Although the −5 dB bandwidth of EOT decreases as β increases, it is still as broad as 1.75 THz at $\beta = 35°$. We emphasize that these results remain valid when β takes minus value. Taking $\beta = -15°$ and 30°, the numerical transmission spectra in Fig. 5(b) are well consistent with the theoretical ones in Fig. 5(a). Taking the frequencies at perfect transmissions, we show the numerical field patterns (in Fig. 5(c)) of one unit cell with periodic boundary along the y-direction. The phase front of transmitted wave exhibits the same tilted angle as that of the incident wave. At the middle position of the gap, the FE remains at a hundreds-folds level (in Fig. 5(d)), although it decreases during increasing β. These numerical results further confirm the above theoretical results.

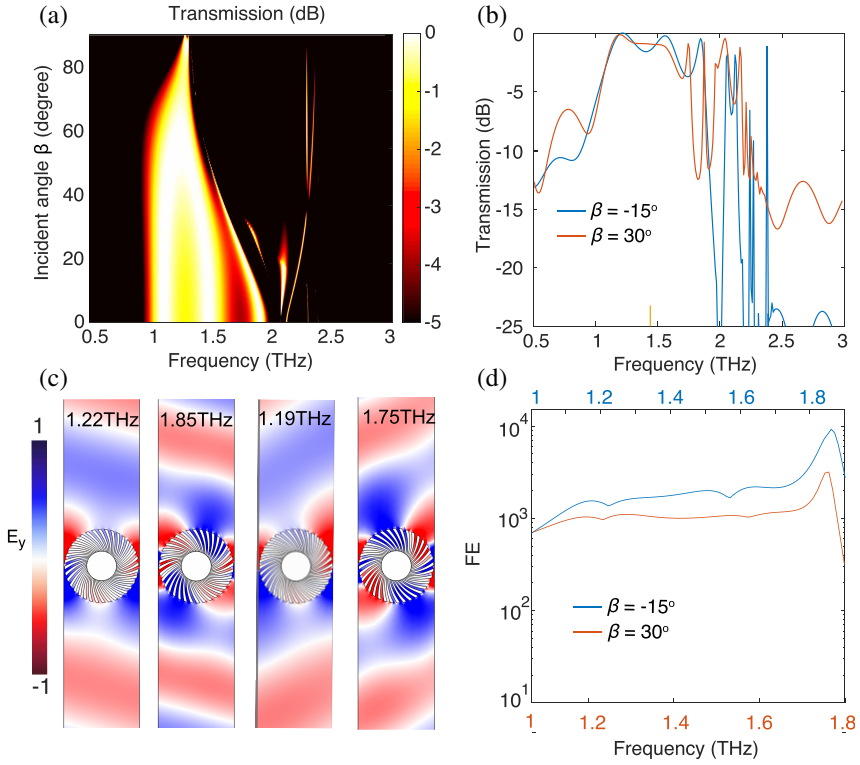

Figure 5. The incidence-angle dependence of EOT and FE. (a) The calculated phase diagram T (β, f). β represents the incidence angles. (b) The simulated transmission spectra under oblique incidence $\beta = -15°$ (blue line), and 30° (red line). (c) Simulated field patterns under oblique incidence $\beta = 15°$ @ 1.22 THz, and 1.85 THz, and $\beta = 30°$ @ 1.19 THz, and 1.75 THz respectively. (d) The field enhancement at the middle of the gap. The lower and upper horizontal axis are for the $\beta = -15°$, and $\beta = 30°$, respectively.

4. CONCLUSION

We proposed designer-plasmonic metagratings for simultaneously realizing broadband EOTs and FEs at THz frequencies. Typically, in the metagrating with spiral angle $\theta = 30°$, the -5 dB bandwidth is 0.96 THz, and the field enhancement is around 7000 times. The broadband EOTs are attributed to the hybridizations between multiple DLSP resonances. The designed metagratings host broadband FEs over a wide range of incident angles. Furthermore, the spiral angle of the groove arms provides an extra degree-of-freedom for designing broadband FE, not attainable in conventional metagratings. Our proposed structure is possible to be realized with modern advanced additive manufacturing technology. These results may promise applications in THz nonlinear effects, THz harvesting, broadband beam-steering, or investigating novel physics, e.g., topological phenomena [38, 39].

ACKNOWLEDGMENT

This work was supported by the Key Research and Development Program of the Ministry of Science and Technology under Grants No. 2022YFA1404902, 2022YFA1404704, and 2022YFA1405200, the National Natural Science Foundation of China (NNSFC) under Grants No. 62171406, 11961141010 and 61901411, the Zhejiang Provincial Natural Science Foundation under Grants No. Z20F010018, National Key Laboratory Foundation No. 6142205200402, the Fundamental Research Funds for the Central Universities No. 2020XZZX002-15.

REFERENCES

1. García de Abajo, F. J., "Colloquium: Light scattering by particle and hole arrays," *Reviews of Modern Physics*, Vol. 79, 1267–1290, 2007.
2. Garcia-Vidal, F. J., L. Martin-Moreno, T. W. Ebbesen, and L. Kuipers, "Light passing through subwavelength apertures," *Reviews of Modern Physics*, Vol. 82, 729–787, 2010.
3. Schuller, J. A., E. S. Barnard, W. Cai, Y. C. Jun, J. S. White, and M. L. Brongersma, "Plasmonics for extreme light concentration and manipulation," *Nature Materials*, Vol. 9, 193–204, 2010.
4. Dombi, P., Z. Pápa, J. Vogelsang, S. V. Yalunin, M. Sivis, G. Herink, S. Schäfer, P. Groß, C. Ropers, and C. Lienau, "Strong-field nano-optics," *Reviews of Modern Physics*, Vol. 92, 025003, 2020.
5. Rajabali, S., E. Cortese, M. Beck, S. De Liberato, J. Faist, and G. Scalari, "Polaritonic nonlocality in light-matter interaction," *Nature Photonics*, Vol. 15, 690–695, 2021.
6. Lu, M. H., X. K. Liu, L. Feng, J. Li, C. P. Huang, Y. F. Chen, Y. Y. Zhu, S. N. Zhu, and N. B. Ming, "Extraordinary acoustic transmission through a 1D grating with very narrow apertures," *Physical Reviwe Letters*, Vol. 99, 174301, 2007.
7. Christensen, J., L. Martin-Moreno, and F. J. Garcia-Vidal, "Theory of resonant acoustic transmission through subwavelength apertures," *Physical Review Letters*, Vol. 101, 014301, 2008.
8. Estrada, H., F. J. Garcia de Abajo, P. Candelas, A. Uris, F. Belmar, and F. Meseguer, "Angle-dependent ultrasonic transmission through plates with subwavelength hole arrays," *Physical Review Letters*, Vol. 102, 144301, 2009.
9. Zhu, J., J. Christensen, J. Jung, L. Martin-Moreno, X. Yin, L. Fok, X. Zhang, and F. J. Garcia-Vidal, "A holey-structured metamaterial for acoustic deep-subwavelength imaging," *Nature Physics*, Vol. 7, 52–55, 2010.
10. Ebbesen, T. W., H. J. Lezec, H. F. Ghaemi, T. Thio, and P. A. Wolff, "Extraordinary optical transmission through sub-wavelength hole arrays," *Nature*, Vol. 391, 667–669, 1998.
11. Hanham, S. M., A. I. Fernandez-Dominguez, J. H. Teng, S. S. Ang, K. P. Lim, S. F. Yoon, C. Y. Ngo, N. Klein, J. B. Pendry, and S. A. Maier, "Broadband terahertz plasmonic response of touching InSb disks," *Advanced Materials*, Vol. 24, OP226–230, 2012.
12. Seo, M. A., H. R. Park, S. M. Koo, D. J. Park, J. H. Kang, O. K. Suwal, S. S. Choi, P. C. M. Planken, G. S. Park, N. K. Park, Q. H. Park, and D. S. Kim, "Terahertz field enhancement by a metallic nano slit operating beyond the skin-depth limit," *Nature Photonics*, Vol. 3, 152–156, 2009.

13. Gómez Rivas, J., C. Schotsch, P. Haring Bolivar, and H. Kurz, "Enhanced transmission of THz radiation through subwavelength holes," *Physical Review B*, Vol. 68, 201306, 2003.
14. Qu, D., D. Grischkowsky, and W. Zhang, "Terahertz transmission properties of thin, subwavelength metallic hole arrays," *Optics Express*, Vol. 29, 896–898, 2004.
15. Azad, A. K. and W. Zhang, "Resonant terahertz transmission in subwavelength metallic hole arrays of sub-skin-depth thickness," *Optics Express*, Vol. 30, 2945–2947, 2005.
16. Rivas, J. G., C. Janke, P. H. Bolivar, and H. Kurz, "Transmission of THz radiation through InSb gratings of subwavelength apertures," *Optics Express*, Vol. 13, 847–859, 2005.
17. Lee, J. W., M. A. Seo, D. H. Kang, K. S. Khim, S. C. Jeoung, and D. S. Kim, "Terahertz electromagnetic wave transmission through random arrays of single rectangular holes and slits in thin metallic sheets," *Physical Review Letters*, Vol. 99, 137401, 2007.
18. Chen, H.-T., H. Lu, A. K. Azad, R. D. Averitt, A. C. Gossard, S. A. Trugman, J. F. O'Hara, and A. J. Taylor, "Electronic control of extraordinary terahertz transmission through subwavelength metal hole arrays," *Optics Express*, Vol. 16, 7641–7648, 2008.
19. Masson, J.-B., A. Podzorov, and G. Gallot, "Extended Fano model of extraordinary electromagnetic transmission through subwavelength hole arrays in the terahertz domain," *Optics Express*, Vol. 17, 15280–15291, 2009.
20. Wu, J., H. Dai, H. Wang, B. Jin, T. Jia, C. Zhang, C. Cao, J. Chen, L. Kang, W. Xu, and P. Wu, "Extraordinary terahertz transmission in superconducting subwavelength hole array," *Optics Express*, Vol. 19, 1101–1106, 2011.
21. Gao, W., J. Shu, K. Reichel, D. V. Nickel, X. He, G. Shi, R. Vajtai, P. M. Ajayan, J. Kono, D. M. Mittleman, and Q. Xu, "High-contrast terahertz wave modulation by gated graphene enhanced by extraordinary transmission through ring apertures," *Nano Letters*, Vol. 14, 1242–1248, 2014.
22. Banerjee, S., N. Lok Abhishikth, S. Karmakar, D. Kumar, S. Rane, S. Goel, A. K. Azad, and D. Roy Chowdhury, "Modulating extraordinary terahertz transmissions in multilayer plasmonic metasurfaces," *Journal of Optics*, Vol. 22, 125101, 2020.
23. Ren, X.-P., R.-H. Fan, R.-W. Peng, X.-R. Huang, D.-H. Xu, Y. Zhou, and M. Wang, "Nonperiodic metallic gratings transparent for broadband terahertz waves," *Physical Review B*, Vol. 91, 045111, 2015.
24. Nguyen, T. K., P. T. Dang, I. Park, and K. Q. Le, "Broadband THz radiation through tapered semiconductor gratings on high-index substrate," *Journal of the Optical Society of America B*, Vol. 34, 583–589, 2017.
25. Song, J., Y. Shi, X. Liu, M. Li, X. Wang, and F. Yang, "Enhanced broadband extraordinary terahertz transmission through plasmon coupling between metal hemisphere and hole arrays," *Optical Materials Express*, Vol. 11, 2700–2710, 2021.
26. Huang, X. R., R. W. Peng, and R. H. Fan, "Making metals transparent for white light by spoof surface plasmons," *Physical Review Letters*, Vol. 105, 243901, 2010.
27. Alu, A., G. D'Aguanno, N. Mattiucci, and M. J. Bloemer, "Plasmonic brewster angle: Broadband extraordinary transmission through optical gratings," *Physical Review Letters*, Vol. 106, 123902, 2011.
28. Subramania, G., S. Foteinopoulou, and I. Brener, "Nonresonant broadband funneling of light via ultrasubwavelength channels," *Physical Review Letters*, Vol. 107, 163902, 2011.
29. Fan, R. H., R. W. Peng, X. R. Huang, J. Li, Y. Liu, Q. Hu, M. Wang, and X. Zhang, "Transparent metals for ultrabroadband electromagnetic waves," *Advanced Materials*, Vol. 24, 1980–1986, 2012.
30. Liao, Z., A. I. Fernández-Domínguez, J. Zhang, S. A. Maier, T. J. Cui, and Y. Luo, "Homogenous metamaterial description of localized spoof plasmons in spiral geometries," *ACS Photonics*, Vol. 3, 1768–1775, 2016.
31. Kong, J. A., *Electromagnetic Wave Theory*, Wiley, 2008.
32. Tsang, L. and J. A. Kong, *Scattering of Electromagnetic Waves*, Vol. III, *Advanced Topics*, Wiley, 2001.

33. Tsang, L., J. A. Kong, K. H. Ding, and C. O. Ao, *Scattering of Electromagnetic Waves*, Vol. II, *Numerical Simulations*, Wiley, 2001.
34. Kushta, T. and K. Yasumoto, "Electromagnetic scattering from periodic arrays of two circular cylinders per unit cell," *Progress In Electromagnetics Research*, Vol. 29, 69–85, 2000.
35. Liang, Z. and J. Li, "Extreme acoustic metamaterial by coiling up space," *Physical Review Letters*, Vol. 108, 114301, 2012.
36. Cheng, Y., C. Zhou, B. G. Yuan, D. J. Wu, Q. Wei, and X. J. Liu, "Ultra-sparse metasurface for high reflection of low-frequency sound based on artificial Mie resonances," *Nature Materials*, Vol. 14, 1013–1019, 2015.
37. Liu, F., S. Zhang, L. Luo, W. Li, Z. Wang, and M. Ke, "Superscattering of sound by a deep-subwavelength solid mazelike rod," *Physical Review Applied*, Vol. 12, 064063, 2019.
38. Yang, Z., F. Gao, X. Shi, X. Lin, Z. Gao, Y. Chong, and B. Zhang, "Topological acoustics," *Physical Review Letters*, Vol. 114, 114301, 2015.
39. Xue, H., Y. Yang, F. Gao, Y. Chong, and B. Zhang, "Acoustic higher-order topological insulator on a kagome lattice," *Nature Materials*, Vol. 18, 108–112, 2019.